# Performance of the Keck Observatory adaptive-optics system

Marcos A. van Dam, David Le Mignant, and Bruce A. Macintosh

The adaptive-optics (AO) system at the W. M. Keck Observatory is characterized. We calculate the error budget of the Keck AO system operating in natural guide star mode with a near-infrared imaging camera. The measurement noise and bandwidth errors are obtained by modeling the control loops and recording residual centroids. Results of sky performance tests are presented: The AO system is shown to deliver images with average Strehl ratios of as much as 0.37 at 1.58 μm when a bright guide star is used and of 0.19 for a magnitude 12 star. The images are consistent with the predicted wave-front error based on our error budget estimates. © 2004 Optical Society of America

*OCIS codes:* 010.1080, 010.1330, 010.7350.

## 1. Introduction

Adaptive optics (AO) has found widespread use in astronomical settings to compensate for atmospheric turbulence and telescope aberrations.[1–3] At the W. M. Keck Observatory there are identical AO systems on the Keck I and Keck II telescopes.[4] Keck I is used only for interferometry and hence does not have a science camera, whereas Keck II supports a number of instruments. In this paper we characterize the performance of the Keck II AO system operating with a natural guide star when it is used with the NIRC2 (near-infrared) camera in imaging mode. The performance of the Keck I AO system is similar.

Characterization of AO systems has been undertaken at other observatories.[5–9] It is important to understand the performance of the AO system under different atmospheric conditions and guide star brightnesses to be able to predict the science output of an observation. Learning to understand the performance of the AO system is also a good exercise to perform in conjunction with an AO optimization effort: knowledge of the error terms leads naturally to their elimination or mitigation. Finally, understanding the performance of current AO systems will lead to better design and implementation of future systems.

The remainder of the paper is as follows: In Section 2 we outline the Keck AO system and its components. This is followed by presentation of an error budget and experimental results in Section 3, and conclusions are drawn in Section 4.

## 2. Keck Adaptive-Optics System

The Keck AO system consists of a tip–tilt mirror (TT), a 349-actuator Xinetics deformable mirror (DM), and a dichroic beam splitter that directs the visible light to the 20 × 20 subaperture Shack–Hartmann wave-front sensor (WFS) and the infrared light to the science camera. There are also two control loops driving the TT and the DM.

The fact that the Keck telescope is on an altitude–azimuth mount with the AO system on a Nasmyth platform means that as the telescope tracks a star, the image rotates on the science camera. To compensate for this rotation there is an image rotator located before the AO system that keeps the image steady as the telescope tracks an object but causes the pupil to rotate on the wave-front sensor camera and on the DM. The 304 subapertures encompass a circular region. Because the pupil is not circular but is a serrated hexagon, the illuminated subapertures change with time. At any given time, 240 of the 304 subapertures are active and are used to reconstruct the wave front. The other subapertures are discarded, as they have little or no illumination.

The science camera is a 1024 × 1024 pixel infrared camera with numerous filters. It also has spectro-

When this research was performed, M. A. van Dam and B. A. Macintosh were with the Lawrence Livermore National Laboratory, P.O. Box 808, Livermore, California 94550. M. A. van Dam (mvandam@keck.hawaii.edu) and D. Le Mignant are now with W. M. Keck Observatory, 65-1120 Mamalahoa Highway, Kamuela, Hawaii 96743.

Received 14 January 2004; revised manuscript received 29 April 2004; accepted 6 July 2004.

0003-6935/04/295458-10$15.00/0

scopic and coronographic capabilities. The camera has a subarraying capability that can be used to reduce the exposure time to as short as 8 ms, with 3 s between consecutive exposures. The plate scale can be selected to be 10, 20, or 40 milli arc seconds (mas).

In addition to science camera images, there are two other forms of data at our disposal with which to characterize the AO system. Telemetry consists of the values of any quantity used by the AO system and is streamed at a rate of 10–20 Hz. It is useful for detecting trends over long periods of time. Telemetry is used by the AO system for many operations, such as off loading focus to the telescope. Diagnostics refers to 1000 consecutive samples of the output of most values calculated by the wave-front controller, such as the centroids and the voltage applied to the DM or the TT. Writing the diagnostics to disk typically takes ~10 s, depending on how many data are stored.

There is also an atmospheric characterization tool that estimates Fried's parameter, $r_0$,[10] from open- or closed-loop telemetry or diagnostics online.[11]

### A. Charge-Coupled Device

The wave-front sensing CCD is a Lincoln Labs MIT 64 × 64 CCD. The readout electronics consists of four amplifiers, one for each of four 64 × 16 strips. There are 3 × 3 pixels that correspond to each subaperture, which consists of a 2 × 2 pixel quad cell with a guard band between adjacent subapertures. To compute the error in estimating the centroid of the WFS spots, one needs to determine some physical parameters of the CCD.

The CCD intensities are measured not in photons but in analog-to-digital units (ADUs). The probability distribution of the number of photons detected by the CCD obeys Poisson statistics, with the variance being equal to the expected number of photons. This property is used to compute the electrons per ADU conversion factor. Wave-front sensing images were captured at the highest frame rate with different neutral-density filters. Each frame was normalized to remove overall intensity fluctuations between frames with the same filter. It can be assumed that the variation from frame to frame is due to intensity fluctuations in the light source rather than to the fluctuations in photon detection. Then the images were flat fielded. The slope of the graph of the variance of the pixel intensities versus the mean pixel intensity gives the inverse of the electrons per ADU factor, which takes a value of 1.99. The third of the four CCD amplifiers exhibits nonlinear behavior. The ADU/electron ratio for that CCD strip increases gradually from ~60% of its maximum value in the limit where there is no light to almost 100% at ~150 ADU counts per subaperture. Because the readout noise in ADU stays the same in the nonlinear strip, the readout noise in electrons is actually higher than in the other strips. We have ensured that no subaperture is straddled by the third CCD strip and a neighboring one.

To find the dark current and the read noise, we captured dark frames at different frame rates. The mean intensity was recorded and plotted as a function of exposure time. The slope of the graph gives the dark current, 4470 (electrons/pixel)/s. Dark current is strongly dependent on temperature, and the CCDs are Peltier cooled to 267 K (−6 °C). The measured dark current is consistent with its theoretical value:

$$I_{\mathrm{dark}} = AT^{3/2} \exp(-E_g/2kT), \tag{1}$$

where $I_{\mathrm{dark}}$ is the dark current, $E_g$ = 1.2 eV is the silicon bandgap energy, $T$ is the temperature in degrees Kelvin, $k$ is Boltzmann's constant, and $A$ is a proportionality constant equal to $2.15 \times 10^8\ e^-\ s^{-1}\ \mathrm{pixel}^{-1}\ \mathrm{K}^{-3/2}$ according to Lincoln Labs.[12] Subtracting the dark-current contribution from frames taken at 672 Hz gives a read noise of 6.5 (electrons/pixel)/readout.

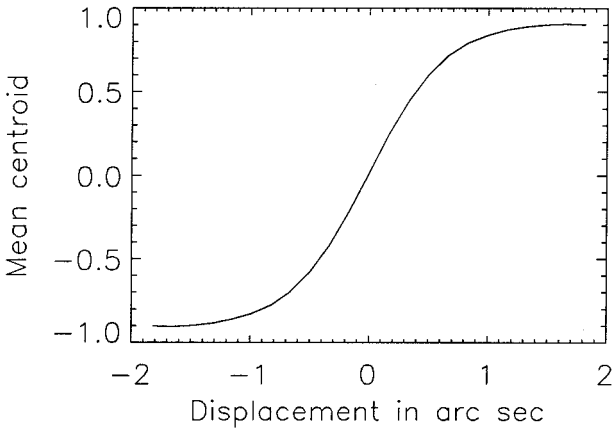


Fig. 1. Transfer curve between the angle of arrival in arc seconds and the mean centroids. The plot is generated by displacement of the white-light source in the $y$ direction.

### B. Lenslets

The lenslet array is a 20 × 20 square array of acrylic lenslets with a pitch of 200 μm obtained from Adaptive Optics Associates. The corners of the lenslets are optically conjugate to the four neighboring actuators in what is commonly called the Fried configuration.[13] There are three sets of lenslet arrays available, with focal lengths of 2.0, 5.0, and 7.9 mm that correspond to design plate scales at the WFS CCD of 2.44, 0.98, and 0.62 arc sec/pixel, respectively. The measured plate scales, however, are 2.4, 0.8, and 0.5 arc sec/pixel.

The WFS spot size is a useful quantity because it is needed to convert the centroid measurements into angles of arrival. Knowing how the size of the spot changes as a result of turbulence is important in eliminating dynamic calibration errors, optimizing the loop gains, and calculating the measurement noise and bandwidth errors.

To find the size of the spots on the WFS, we displace the spots over a range of values and measure the centroid, as shown in Fig. 1.

The maximum slope $m$ of the displacement in arc seconds–versus–centroid plot is related to the FWHM of a Gaussian spot by

$$\mathrm{FWHM} = 2 \times 2.355/\sqrt{2\pi m}. \quad (2)$$

One can shift the spot by scanning the artificial light source across the focal plane of the telescope and measuring the centroids.[11] One finds the displacement of the spot by multiplying the displacement of the light source by the plate scale at the focal plane. An alternative way to scan the spot is to close the DM and TT loops and add a range of constants from say, $-0.1$ to 0.1 to all the $x$ (or the $y$) centroid offsets. The displacement of the spot is then measured with the science camera, which has an extremely well-calibrated plate scale. The latter method has the advantage that it can also be used to measure the spot size on the sky by use of a guide star.

The FWHM spot sizes on the light source were found to be 1.25, 0.52, and 0.40 arc sec for the 2.4-, 0.8-, and 0.5-arc-sec plate scales, respectively. These sizes are to be compared with a diffraction-limited spot size of 0.23 at 700 nm. We can well explain the discrepancy by postulating that the measured intensity is a convolution of a diffraction-limited spot and a Gaussian with a FWHM of half a pixel. The blurring of the spot is almost certainly due to charge diffusion, and the extent of the charge diffusion is consistent with other measurements of similar CCDs.[14] The effect of the charge diffusion on the spot size increases with increasing plate scale.

Under average seeing conditions ($r_0$ of $\sim$0.2 m at 500 nm, estimated by use of the atmospheric characterization tool[11]), the average spot size increases relative to the spot that uses the white-light source by 25% and 70% for the 2.4- and 0.8-arc-sec plate scales, respectively.

Usually the 2.4-arc-sec plate scale lenslets are used because the spot size does not change much in the presence of turbulence. Also, using a lenslet with a large plate scale means that essentially all the light is detected by the pixels in the quad cells, and little light leaks out to the guard bands. However, the larger the angular extent of the spot, the higher the noise on the wave-front slope estimates. Although the error in the centroid estimate is independent of spot size, the wave-front slope that corresponds to this error is proportional to the spot size. Hence, when the guide star is faint and the seeing is relatively good, the 0.8-arc-sec plate scale is preferred. The 0.5-arc-sec plate scale is never used.

When the DM is nominally flat, the rms centroid measurements are 0.11 centroid (0.068 arcsec) on the 2.4-arc-sec plate scale and 0.13 centroid (0.028-arc sec) on the 0.8-arc-sec plate scale. These centroid errors are randomly distributed and are believed to stem from the lenslets themselves. As a result of these aberrations and also of aberrations on the science camera leg, the wave-front sensor operates off null. The penalties paid for operating off null are an increase in noise because the WFS is no longer operating in the steepest part of the transfer curve (Fig. 1) and dynamic calibration errors as explained in Subsection 3.F below that are due to the WFS spot size obtained with a calibration source that differs from that obtained with the guide star.

### C. Deformable Mirror

The Keck AO system consists of a Xinetics 349-actuator DM. Oppenheimer *et al*. investigated the influence function of this mirror.[15] The influence function describes the optical effect of the deformation of the mirror when 1 V is applied to the preamplifier. It was calibrated at the Keck Observatory in three ways: by measurement of the wave front directly with an interferometer, by reconstruction of the wave front from the centroids when an actuator is poked, and by defocusing of the calibration source by a known amount and reading the voltage of the actuators. The influence function, $S(x, y)$, can be well approximated by use of the difference of two Gaussians:

$$S(x, y) = \left\{ \frac{w_1}{2\pi\sigma_1^2} \exp\left[\frac{-(x^2 + y^2)}{2\sigma_1^2}\right] + \frac{w_2}{2\pi\sigma_2^2} \exp\left[\frac{-(x^2 + y^2)}{2\sigma_2^2}\right] \right\} 0.470\ \mu\mathrm{m}. \quad (3)$$

The values for the constants are $w_1 = 2$, $w_2 = -1$, $\sigma_1 = 0.54$ subaperture, and $\sigma_2 = 0.85$ subaperture. It is apparent that the behavior of the DM is more complex than a linear sum of the influence functions of the actuators. For example, if all the actuators have the same voltage applied, the DM produces a piston, which is not predicted by Eq. (3).[16]

### D. Calibration

Calibrating an AO system well is crucial to obtaining good performance on the sky. Here a brief description of the most important calibration procedures is presented. Some of these procedures are reported in more detail elsewhere.[17] The calibrations are performed with a white-light source that is 10 $\mu$m (13.8 mas) in diameter and located at the focus of the telescope.

#### *1. Deformable Mirror-to-Lenslet Registration*

It is important to have the correct registration between the DM and the lenslet. Otherwise the waffle mode, in which actuators are lined up in a checkerboard pattern, would be observed on the DM when the loop were closed. The algorithm used to perform the DM-to-lenslet registration is adapted from a paper of Oliker.[18] It involves putting a waffle on the DM and moving the lenslets to minimize the signal sensed by the WFS.

#### *2. Focusing the Wave-Front Sensor's Charge-Coupled Device*

Previously, one focused the CCD by defining the focus to be the position of the CCD where the steepest transfer curve (see Fig. 1) occurs. It is easy to show

that this is indeed the best focus when there is no charge diffusion on the CCD but differs greatly from the true focus in the presence of charge diffusion. Instead, a waffle pattern is introduced into the DM. This is equivalent to adding 45° astigmatism to each lenslet. If the CCD is out of focus, the spots on the WFS will be more elongated along one diagonal and not the other. At the best focal position the spots will be symmetrical.

#### 3. System Matrix Generation

The system matrix relates the motion of each actuator to the centroids produced at the WFS. One calculates it by moving each actuator by $\pm 0.2$ μm and recording the difference in the centroids. Centroids that correspond to subapertures that are more than twice the subaperture spacing away from the actuator are set to zero to reduce the level of noise. The actuator motion is chosen such that it yields a good signal-to-noise ratio in the centroid measurements while ensuring that the WFS is operating in its linear range.

#### 4. Image Sharpening

There are aberrations on the imaging leg that are not sensed by the WFS and vice versa. In the absence of any external aberrations, one would want the DM to have the shape that maximizes the Strehl ratio. Image sharpening refers to the process of finding this optimum shape of the DM. The noncommon path aberrations are calibrated as follows: First the DM is flattened. The phase on the DM is measured with a WYKO phase-shifting interferometer and a voltage is applied to cancel the measured phase.[17] Unfortunately, the interferometer does not sense some of the actuators at the edges, and these cannot be flattened properly. Next, the phase-diversity algorithm of Loefdahl and Scharmer[19] is employed to remove the Zernike polynomials[20] up to $Z_{15}$. Typically, 100 nm of rms wave-front error is applied to the DM to correct for any aberrations in the imaging leg and in the common path. The algorithm reduces the total wave-front error seen on the artificial source from 150 to 113 nm. The phase-diversity algorithm is applied only to images taken at one location in the camera and with one filter. Hence there are additional field- and filter-dependent wave-front errors.

Once the optimum shape is found, it is placed on the DM and the centroids measured by the wave-front sensor are defined to be the centroid origins. In closed-loop operation, the DM and the TT are driven in such a way as to null the difference between the centroids and the centroid origins. Hence if the loops are immediately closed, the DM should not move.

Under average atmospheric conditions ($r_0 = 20$ cm), the spot obtained with the 2.4-arc-sec/pixel plate scale increases in size from 1.25 to 1.55 arc sec. Before going to the sky, the centroid offsets are scaled by 0.8 to account for the increase in spot size. If the beacon is an extended source, such as a planet, or if the 0.8-arc-sec/pixel plate scale is used, the centroid offsets are scaled even more. Unfortunately, the spot size is constantly changing as the seeing changes. It is intended that in the near future the spot size will be monitored in real time.[21]

### E. Signal Processing

The wave-front controller can operate at frame rates ranging from 55 to 672 Hz. The upper limit is set by the combination of the camera readout time and the speed at which the computers can multiply the reconstructor matrix by the centroid measurements. There are separate control loops for the TT and the DM. The computed delay times, from the time that the CCD is read until the time that the TT and DM voltages are updated, are 1.65 and 2.13 ms, respectively.

#### 1. Reconstruction Matrix

The pupil rotates as the telescope tracks an object, and the illuminated subapertures change with time. Every time the pupil rotates 1°, the calculation of a new reconstruction matrix is triggered. Until recently the matrix inversion of the influence matrix, $H$, was performed with a singular value decomposition algorithm.[22] This has been replaced by a Bayesian reconstructor that uses the covariances of Kolmogorov turbulence, $C_\phi$, and the relative noise in each subaperture, $W$, as prior information. There is a parameter, α, that can be adjusted depending on the signal-to-noise ratio. The reconstructor, $R$, is given by[23]

$$R = (H^T W^{-1} H + \alpha C_\phi^{-1})^{-1} H^T W^{-1}. \quad (4)$$

This would be the optimal reconstructor in the open-loop case; simulations and extensive sky testing have demonstrated that it also performs well in a closed loop. The reason that it works well is that the inversion of the system matrix is regularized such that noise in the centroids leads to smaller actuator motions. The new reconstructor has resulted in an increase in the Strehl ratio corresponding to the elimination of 100 nm of wave-front error (in quadrature) for bright guide stars. The most salient difference is the elimination of the four spots in a square pattern in the image that are indicative of unsensed waffle on the DM. The magnitude of the improvement increases as the guide stars get fainter because α is increased to further suppress the noise at the expense of suppressing some signal.

#### 2. Loop Gains and Compensator

Each of the control loops has its own controller. The TT loop is a straight integrator with a variable loop gain, $k_{TT}$, and a fixed gain scaling of 0.8:

$$y[n] = y[n-1] + 0.8 k_{TT} u[n], \quad (5)$$

where $y[n]$ is the output from and $u[n]$ is the input to the controller at time $n$. The transfer function can be written as

$$H_{\mathrm{TT}}(z) = \frac{0.8k_{\mathrm{TT}}z}{z-1}, \tag{6}$$

where $z$ is the complex $Z$-transform variable. The DM loop has a double pole compensator with the following temporal response:

$$e[n] = -we[n-1] + k_{\mathrm{DM}}u[n], \tag{7}$$

$$y[n] = ly[n-1] + e[n], \tag{8}$$

where $e[n]$ is an intermediate quantity. The transfer function is

$$H_{\mathrm{DM}}(z) = \frac{k_{\mathrm{DM}}z^2}{(z-l)(z+w)}. \tag{9}$$

The compensator, whose function is to increase the bandwidth of the controller,[24] has its weight, $w$, set to 0.25. The leak factor, $l$, which is set to 0.999 for bright stars and to 0.99 otherwise, ensures that invisible modes do not build up in the DM. The loop gain, $k_{\mathrm{DM}}$, is also variable.

The optimum loop gains depend on the turbulence strength and speed, the extent and brightness of the guide star, and the frame rate. In routine operation the loop gains and the frame rate are set by use of a lookup table that has the median number of ADUs per subaperture per second as its only input. We plan to implement real-time gain optimization by using centroid telemetry.

## 3. Error Budget

An error budget consists of a breakdown of the wave-front error into individual components. It is important to know the magnitude of the individual error terms because this knowledge can be used to place more resources in reducing the larger sources of error. In addition, the image quality can be predicted in advance if the error budget as a function of seeing and guide star magnitude is known.

### A. Strehl Ratio

A figure of merit often used to characterize the error of an AO system is the Strehl ratio, $S$. It is defined as the ratio of the maximum value of the measured point-spread function to the maximum value of the diffraction-limited point-spread function. The Strehl ratios of all the images were calculated by use of a window with a diameter of 2 arc sec.

The Strehl ratio is related to the wave-front errors through the Maréchal approximation[3]:

$$S = \exp(-\sigma_\phi{}^2)\exp(-\sigma_\chi{}^2), \tag{10}$$

where $\sigma_\phi{}^2$ is the wave-front phase variance and $\sigma_\chi{}^2$ is the variance of the log-normal amplitude at the pupil plane. An AO system with a single wave-front corrector conjugate to the ground can correct only the wave-front phase aberrations. Hence the goal of the AO system is to minimize the wave-front error. In this section, the individual wave-front error terms are presented. The phase error is inversely proportional to the wavelength, so the Strehl ratio increases with increasing wavelength. In engineering tests, the filter used was the $H$ continuum, a narrowband filter centered at 1.58 μm with a 1% passband. A short wavelength enables one to discern performance changes in real time more easily, as the image quality varies more than for the longer wavelengths. All Strehl ratios quoted in this paper correspond to 1.58 μm. Strehl ratios at other wavelengths can be estimated by use of Eq. (10). All the wave-front errors are rms errors.

### B. Scintillation

The result of propagating an aberrated wave front from height $h$ above the telescope to the primary mirror of the telescope is that the wave-front aberrations, when they are propagated, give rise to changes in the amplitude of the wave. Consider the atmospheric turbulence to be located at a single layer such that the $C_n{}^2$ profile can be written as a delta function at height $h$. Then, for an infinite aperture, it can be shown that the log-normal amplitude variance is given by[25]

$$\sigma_\chi{}^2 = 0.288(\sqrt{\lambda h}/r_0)^{5/3}. \tag{11}$$

Analytic calculations[25] and numerical simulations by the present authors who used Fresnel propagation both show that this result also holds for large astronomical telescopes. For example, consider the hypothetical case of a turbulent layer with $r_0$ values of 20 cm at 500 nm and 80 cm at 1.58 μm located 3 km above the ground. Substituting these values into Eq. (11) gives $\sigma_\chi{}^2 = 0.0048$. The reduction in Strehl ratio when Eq. (10) is used is 0.48%. Inasmuch as virtually all the atmospheric turbulence is below a height of 10 km and the log-amplitude variance depends on $h^{5/6}$, we conclude that the effect of scintillation is negligible compared with that of the wave-front phase.

### C. Camera Errors

The Strehl ratio measured in the artificial light source after image sharpening is 0.77, corresponding to 130 nm of wave-front error. However, the light source can be resolved, and its extent reduces the Strehl ratio by the same amount as 64 nm of wave-front aberrations. Hence the actual wave-front error is 113 nm. Figure 2 shows the phase error after image sharpening computed with the Gerchberg–Saxton phase-retrieval algorithm.[26] Because of the symmetry of the aperture, there is an ambiguity about the sign and the orientation of the phase, so it is difficult to feed back this information in the image sharpening process.[27] It can be seen that most of the residual error consists of high-order aberrations.

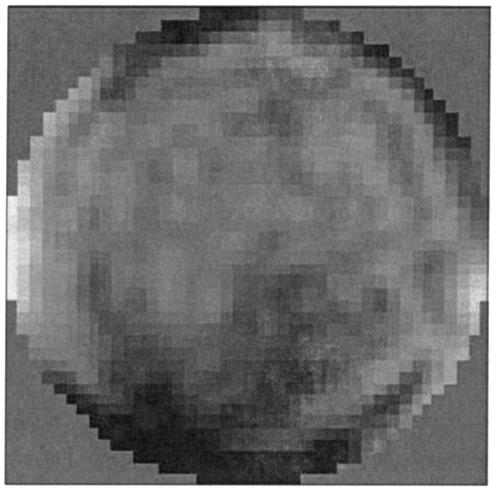

Fig. 2. Phase map of the residual error after image sharpening.

### D. Fitting Error

The fitting error is defined to be the component of the wave-front that cannot be corrected by the DM. There are two sources of wave-front error that the DM has to correct for: atmospheric turbulence and the telescope. The fitting error depends on the spacing between the actuators, the influence function of the actuators, the spatial power spectrum of the wave-front aberrations induced by the turbulence, and the telescope.

Using the influence function described by Eq. (3), we found by simulation that the rms fitting error, $\sigma_{\mathrm{FIT}}$, for Kolmogorov turbulence is $33.2 r_0^{-5/6}$ nm. The general form of the fitting error is given by[3]

$$\sigma_{\mathrm{FIT}} = \sqrt{a_f}\left(\frac{d}{r_0}\right)^{5/6}\frac{\lambda}{2\pi}, \tag{12}$$

where $d$ is the spacing between the actuators, $\lambda$ is the wavelength at which $r_0$ is measured, and $a_f$ is a constant that depends on the influence function. The value of $a_f$ calculated here is 0.46, which is higher than the range 0.28–0.34 presented by Hardy for a continuous-plate mirror.[3]

The Keck primary mirror consists of 36 hexagonal segments. Each segment has low-order aberrations and a dimple in the center that results from the manufacturing process. In addition, there are stacking (piston) and pointing (tip–tilt) errors of each segment relative to its neighbors. It is estimated that after phasing of the mirror segments[28] there is ~110 nm of wave-front residual error. We found the telescope fitting error, $\sigma_{\mathrm{TEL}}$, after correction by the DM to be 60 nm by simulating the errors on the primary mirror of the telescope: It is not possible to correct well for the segment discontinuities. The segments are not routinely phased before an AO run, so this error could be greater.

### E. Bandwidth and Noise Errors

The bandwidth errors are due to the finite sampling rate of the atmospheric turbulence and to the delay between the centroid measurements and the DM and TT command updates. The source of the noise errors is the uncertainty in the centroid estimates that is due to the finite number of photons on the WFS. To calculate these error terms requires a good model of the temporal response of the control loop.

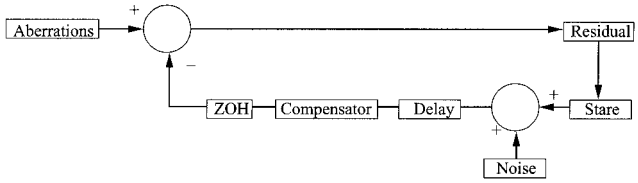


Fig. 3. Schematic of the control loop. The diagnostics measure the centroids immediately after addition of the noise, and the mirror is driven by the signal coming from the zero-order hold.

#### 1. *Modeling the Dynamic Performance of the AO System*

The wave-front controller is described in detail by Johansson *et al.*,[29] and the features of the controller required in the model are simply stated here. A schematic of the TT and DM feedback loops for the Keck AO system is displayed in Fig. 3. Both loops have a similar form, but the compensators and the compute delays differ. "Stare" (camera stare) refers to the act of integrating the signal on the wave-front sensor for one cycle. "ZOH" (zero-order hold) refers to the fact that a constant (zero-order) voltage is placed on the TT or the DM for the duration of one cycle. Even though these two processes are physically different, they have the same transfer function.

The transfer functions of the individual blocks are[24]

- Camera stare and the zero-order hold with period $T$:

$$H_{\mathrm{Stare}}(s) = H_{\mathrm{ZOH}}(s) = \frac{1-\exp(-sT)}{sT}. \tag{13}$$

- Compute delay with delay time $\tau_c$:

$$H_{\mathrm{Delay}}(s) = \exp(-s\tau_c). \tag{14}$$

We model the compensator block by substituting $z = \exp(sT)$ into the discrete compensator of Eqs. (6) and (9). In Eqs. (13) and (14), $s = i2\pi f$ is the complex frequency variable and $f$ is the frequency. In what follows, all the blocks are written with $f$ as the argument, as $f$ has a more intuitive meaning than $s$ and is computed directly from the discrete Fourier transform of the diagnostics.

The transfer function of the entire feedback arm of either the TT or the DM loop, $H(f)$, can be written as the product of the transfer functions of all the blocks:

$$H(f) = H_{\mathrm{Stare}}(f)H_{\mathrm{Delay}}(f)H_{\mathrm{TT/DM}}(f)H_{\mathrm{ZOH}}(f). \tag{15}$$

There are two inputs into the control system: the noise, $N(f)$, which is assumed to have the same

power at all temporal frequencies, and the turbulence, $X(f)$. We consider two outputs, the mirror position, $M(f)$, and the residual mirror commands obtained from the diagnostics, $D(f)$. The position of the diagnostics in the control loop is just after the addition of the noise, whereas the mirror position is just after the zero-order hold. We obtain the residual DM commands by matrix multiplying the reconstruction matrix by the residual centroids. Likewise, we obtain the residual TT commands by taking the average of the $x$ and $y$ centroids. For notational simplicity we consider the noise to be input before, rather than after, the stare. This assumption has little effect on the transfer function of the control loops.

The mirror position and the diagnostics are related to the turbulence and the noise by the following transfer functions:

$$M(f) = \frac{H(f)}{1 + H(f)}\,[X(f) + N(f)], \tag{16}$$

$$D(f) = \frac{1}{1 + H(f)}\,[X(f) + N(f)]. \tag{17}$$

The measurement noise wave-front error, $\sigma_{\text{Noise}}$, is due to noise in the centroid measurement propagating to the mirror, $N(f)H(f)/[1 + H(f)]$. The square of its value is

$$\sigma_{\text{Noise}}{}^2 = \int_{-\infty}^{\infty} \left| \frac{H(f)}{1 + H(f)} \right|^2 |N(f)|^2 \mathrm{d}f. \tag{18}$$

Inasmuch as the noise has power only at discrete frequencies, Eq. (18) can be rewritten as

$$\sigma_{\text{Noise}}{}^2 = \sum \left| \frac{H(f)}{1 + H(f)} \right|^2 |N(f)|^2, \tag{19}$$

where the summation is over all the sampled discrete frequencies.

The bandwidth error, $\sigma_{\text{BW}}$, is due to the turbulence that is not compensated for by the AO system, $X(f)/[1 + H(f)]$. The diagnostics measure this term with an added noise term that is due to the noise on the centroid measurement propagating through the control loop, as can be seen from Eq. (17). Assuming that the noise and the bandwidth errors are statistically uncorrelated, the bandwidth squared error is

$$\begin{aligned}
\sigma_{\text{BW}}{}^2 &= \int_{-\infty}^{\infty} \left| \frac{1}{1 + H(f)} \right|^2 |X(f)|^2 \mathrm{d}f \\
&= \int_{-\infty}^{\infty} \left[ |D(f)|^2 - \left| \frac{1}{1 + H(f)} \right|^2 |N(f)|^2 \right] \mathrm{d}f \\
&\approx \sum \left[ |D(f)|^2 - \left| \frac{1}{1 + H(f)} \right|^2 |N(f)|^2 \right].
\end{aligned} \tag{20}$$

It follows that one can use knowledge of the transfer function of the AO loop, $H(f)$, and the power spectra of the diagnostics, $|D(f)|^2$, and of the noise, $|N(f)|^2$, to calculate both the bandwidth and the noise error terms.

*2. Calculating the Centroid Variance*

To estimate the noise and bandwidth errors, we must first derive the error in the centroid estimates. Let $I_1$ denote the background-subtracted intensity of one of the pixels in a quad cell. Then its expected value is

$$E[I_1] = pT, \tag{21}$$

and, assuming Gaussian statistics, its variance is

$$\mathrm{Var}(I_1) = (p + d + b)T + \sigma_r{}^2, \tag{22}$$

where $T$ is the integration time, $p$, $d$, and $b$ are the photon, dark-current, and background fluxes in (electrons/pixel)/s, and $\sigma_r$ is the read noise standard deviation in (electrons/pixel)/readout. In the analysis that follows, $d = 4470$, $b = 0$, and $\sigma_r{}^2 = 39.7$. To obtain a simple expression for the variance of the centroid estimates, we make two simplifying assumptions: that there is an equal amount of light in each pixel (i.e., that the average centroid is zero) and that the variance of the denominator in the centroid calculation can be neglected. Then the variance of the $x$ (or the $y$) centroid estimate, $c_x$ (or $c_y$), is

$$\mathrm{Var}(c_x) = \frac{\mathrm{Var}(I_1)}{4E[I_1]^2} = \frac{\mathrm{Var}(I_1)}{4(pT)^2} = \frac{(p + d + b)T + \sigma_r{}^2}{4(pT)^2}. \tag{23}$$

The measured centroid variances agree with Eq. (23). From the variance of the centroids, we can calculate the errors in the TT and DM loops.

*3. Calculating the Tip–Tilt Noise Power Spectrum*

The tip (or tilt) signal sent to the compensator is the average $x$ (or $y$) centroid value over the 240 active subapertures. Hence the sum of the variance of the tip and tilt estimates in centroid units is $2\,\mathrm{Var}(c_x)/240$. The next step is to convert this variance into units of wave-front error. Using Eq. (2), we obtain the result that 1 arc sec is equivalent to 1.2 centroid units for a spot size of 1.55 arc sec. For the Keck telescope the rms wave-front error that is due to a tip or a tilt of 1 arc sec is 12.68 μm. Hence the TT noise's power spectrum is

$$|N_{\text{TT}}(f)|^2 = \frac{2}{240} \left( \frac{12.68}{1.2} \right)^2 \mathrm{Var}(c_x). \tag{24}$$

*4. Calculating the Deformable Mirror Noise's Power Spectrum*

To calculate the deformable mirror noise's power spectral density we must convert centroid units into wave-front units. The residual centroids are multiplied by the reconstruction matrix, $R$, to convert to voltage commands. The voltage commands are then convolved with the actuator influence function, $S$, to

yield the wave front induced by the noise, which is achieved by matrix multiplication. Finally, because for median seeing conditions the size of the WFS spots on the sky increases by 25% relative to the size of the spots on the light source, the wave front must be multiplied by 1.25. As the noise on different centroid measurements is uncorrelated, we can write

$$|N_{\mathrm{DM}}(f)|^2 = 1.25^2 |RS|^2 \,\mathrm{Var}(c_x). \tag{25}$$

*5. Calculating the Bandwidth and Noise Errors*

To calculate the residual power spectra, one must convert the centroids from the diagnostics into TT and DM wave-front aberrations in exactly the same way as the noise is converted. Then the power spectrum of the diagnostics is taken by use of the discrete Fourier transform (DFT):

$$|D(f)|^2 = |\mathrm{DFT}[d[n]w[n]]|^2, \tag{26}$$

where $w[n]$ is a normalized windowing function used to prevent spectral leakage caused by the nonperiodicity of $d[n]$, the residual wave front as measured by the diagnostics. The window must be scaled to have unit power.

We calculate the TT and DM noise errors by inserting Eqs. (24)–(26) into Eq. (19) and relation (20).

Plots of the TT and DM power spectral densities averaged over four sets of diagnostics taken on 15 June 2003 are displayed in Fig. 4. The noise on the diagnostics that we must subtract to obtain the bandwidth error is superimposed. For these data the average rms bandwidth errors were 75 nm for the TT and 103 nm for the DM, with corresponding noise terms of 9 and 17 nm. The guide star is a 7.2 magnitude star.

The power spectral densities are consistent with what one expects by modeling the transfer function of the system.[29] From the plots of the power spectra it can be seen that there are vibration peaks at frequencies ranging from 20 to 40 Hz superimposed upon Kolmogorov turbulence.

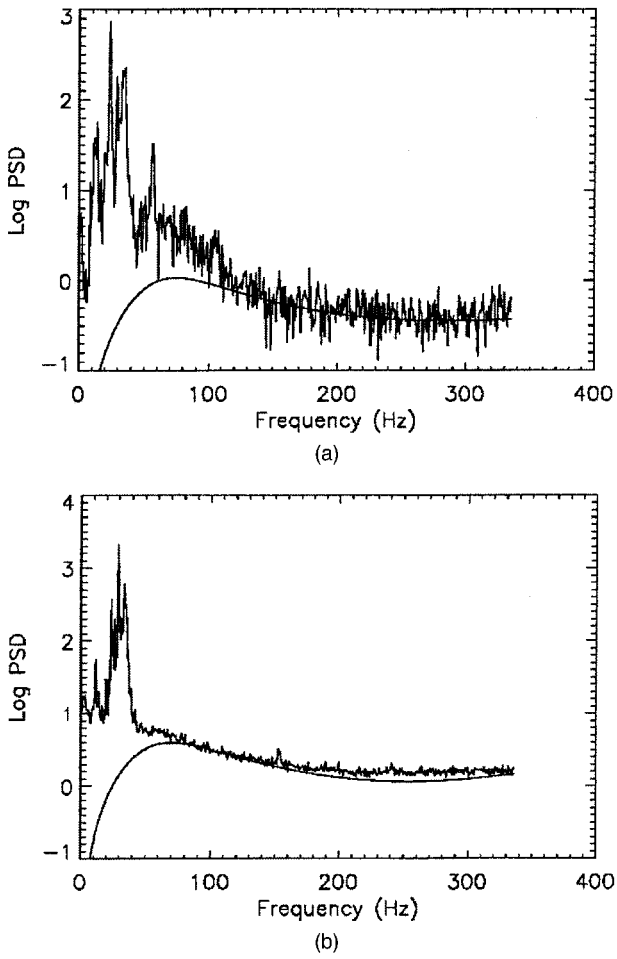


Fig. 4. Logarithm of the power spectral density (in square nanometers per hertz) for the (a) TT and (b) the DM. The smooth curves represent the noise power on the diagnostics.

### F. Miscellaneous Error

Wave-front sensing and reconstruction restrict the performance of the DM. For example, whereas all the actuators were assumed to be independently controlled in the calculation of the fitting errors, in actual fact many of the actuators have no neighboring subapertures and are slaved to the average value of their neighboring actuators. Also, because the wave-front reconstructor has no knowledge of either the influence function of the DM actuators or the analogous response function of the wave-front sensor, even in the absence of noise the actuators are not driven to their optimum values. Even if the DM had an infinite number of degrees of freedom, there would be an error associated with the finite number of measurements.

Because the wave-front sensor measures the average wave-front slope over the subaperture, any wave-front aberrations with a spatial frequency higher than the Nyquist criterion will be aliased to a lower spatial frequency, resulting in an error in the wave-front estimate. This term has a magnitude of approximately one third of the fitting error.[30]

The primary mirror segments are not phased before AO science nights; an estimate of the alignment of the segments is needed. There are static calibration errors: The centroid offsets, the system matrix, and the DM-to-lenslet registration all have some error associated with them. In addition, there are dynamic calibration errors. As the spot size increases owing to the seeing, the offset centroids no longer correspond to the same wave-front slope for which they were calibrated. This error is accounted for to some degree by scaling the centroid offsets, but the scaling is not exact because each spot is of a different size at any given time.

### G. Summary of Error Terms

In calculating the error terms, we assume that the atmospheric turbulence is Kolmogorov,[31] with a turbulence strength defined by $r_0$. Tests have shown that the Kolmogorov model of atmospheric turbu-

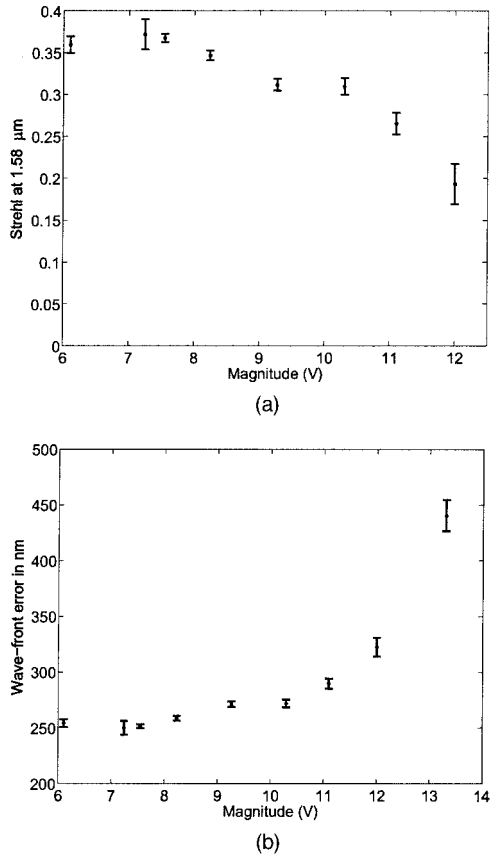


Fig. 5. (a) Strehl ratio at 1.58 μm and (b) the rms wave-front error obtained from the Maréchal approximation. The points represent the mean of ~10 images, and the error bars represent the 1σ spread about the mean.

lence describes the wave-front aberrations encountered at the Keck Observatory well, with the exception of tip–tilt aberrations, which are augmented by telescope vibrations.[11] Hence the measurements of $r_0$ are made from tip–tilt-removed images or centroid diagnostics.

It is important to emphasize that the individual wave-front errors are assumed to be statistically uncorrelated; hence their magnitudes are added in quadrature (i.e., their variances are added). This means that small errors have a negligible effect on the total error budget in the presence of much larger terms.

Many images and diagnostics were taken on 15 June 2003 by use of one guide star with a magnitude of 7. From the Strehl of the images, the rms wave-front error was estimated to be 260 nm. It was estimated that $r_0$ at 500 nm was 18 cm.

To find the total rms wave-front error, we add the variances of all the individual terms in quadrature:

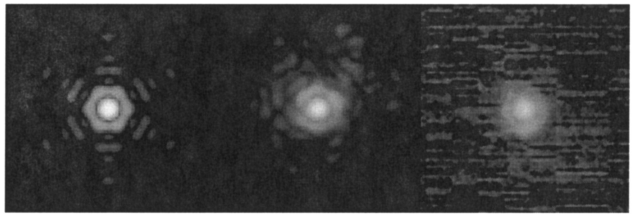

Fig. 6. Left, diffraction-limited image at 1.58 μm; center, best bright star image; right, best image of a magnitude 12 star.

It is reasonable to assume that the miscellaneous error terms presented in Subsection 3.F constitute the 125 nm needed to produce the 260 nm of error estimated from the images.

In addition, images of a number of stars of different brightnesses under a variety of seeing conditions were captured from 22 May to 16 June 2003. Figure 5 plots the Strehl with the $H$ continuum (1.58-μm) filter used as a function of guide star's brightness and the corresponding rms wave-front error from the Maréchal approximation. In each case the optimum lenslet array plate scale, frame rate, and loop gains were chosen. The FWHM of the best corrected images is 36.5 mas, whereas the best images on the magnitude 12 star had a FWHM of 40 mas. By comparison, the diffraction-limited FWHM is 33.6 mas. The magnitude 13.3 star in Fig. 5 was imaged at K′ (2.12 μm) and hence is not included in the Strehl plot. The images had exposure times of 3–20 s. The limiting magnitude of the AO system is ~14.

## 4. Conclusions

The adaptive-optics system at the W. M. Keck Observatory has been characterized. The AO system has been shown to deliver images with an average Strehl ratio of as much as 0.37 at 1.58 μm with a bright guide star; this corresponds to a wave-front error of 260 nm. A bright guide star error budget that is consistent with the observed image quality was presented. The major error terms on a bright guide star are the fitting error, the deformable-mirror bandwidth errors, and the internal calibration error, all of which are more than 100 nm rms. Of secondary importance are the tip–tilt bandwidth error and the telescope aberrations. The limiting magnitude of the AO system is 14, with rapid performance degradation for guide stars fainter than magnitude 12.

This study was performed under the auspices of the U.S. Department of Energy by the University of California, Lawrence Livermore National Laboratory (LLNL), under contract W-7405-Eng-48. The study was supported by the National Science Foundation Science and Technology Center for Adaptive Optics, managed by the University of California at Santa

$$\begin{aligned}\sigma_{\text{total}} &= (\sigma_{\text{CAM}}{}^2 + \sigma_{\text{FIT}}{}^2 + \sigma_{\text{TEL}}{}^2 + \sigma_{\text{TT-BW}}{}^2 + \sigma_{\text{DM-BW}}{}^2 + \sigma_{\text{TT-Noise}}{}^2 + \sigma_{\text{DM-Noise}}{}^2)^{1/2} \\ &= (113^2 + 139^2 + 60^2 + 75^2 + 103^2 + 9^2 + 17^2)^{1/2} \\ &= 229 \text{ nm}. \end{aligned} \tag{27}$$

Cruz under cooperative agreement AST-9876783. The authors thank the AO groups at both the LLNL and the Keck Observatory for their assistance.

## References


1. F. Roddier, ed. *Adaptive Optics in Astronomy* (Cambridge U. Press, Cambridge, UK, 1999).
2. M. C. Roggemann and B. Welsh, *Imaging through Turbulence* (CRC Press, Boca Raton, Fla., 1996).
3. J. W. Hardy, *Adaptive Optics for Astronomical Telescopes* (Oxford U. Press, New York, 1998).
4. P. L. Wizinowich, D. S. Acton, C. Shelton, P. Stomski, J. Gathright, K. Ho, W. Lupton, K. Tsubota, O. Lai, C. Max, J. Brase, J. An, K. Avicola, S. Olivier, D. Gavel, B. Macintosh, A. Ghez, and J. Larkin, "First light adaptive optics images from the Keck II telescope: a new era of high angular resolution imagery," Publ. Astron. Soc. Pac. **112,** 315–319 (2000).
5. M. A. van Dam and B. A. Macintosh, "Characterization of adaptive optics at Keck Observatory," in *Astronomical Adaptive Optics Systems and Applications*, R. K. Tyson and M. Lloyd-Hart, eds., Proc. SPIE **5169,** 1–10 (2003).
6. M. Troy, R. G. Dekany, G. L. Brack, B. R. Oppenheimer, E. E. Bloemhof, T. Trinh, F. G. Dekens, F. Shi, T. L. Hayward, and B. R. Brandl, "Palomar adaptive optics project: status and performance," in *Adaptive Optical Systems Technology*, P. L. Wizinowich, ed., Proc. SPIE **4007,** 31–40 (2000).
7. F. Rigaut, D. Salmon, R. Arsenault, J. Thomas, O. Lai, D. Rouan, J. P. Véran, P. Gigan, D. Crampton, J. M. Fletcher, J. Stilburn, C. Boyer, and P. Jagourel, "Performance of the Canada–France–Hawaii telescope adaptive optics Bonnette," Publ. Astron. Soc. Pac. **110,** 152–164 (1998).
8. L. C. Roberts, Jr. and C. R. Neyman, "Characterization of the AEOS system," Publ. Astron. Soc. Pac. **114,** 1260–1266 (2002).
9. D. Gavel, E. Gates, C. Max, S. Olivier, B. Bauman, D. Pennington, B. Macintosh, J. Patience, C. Brown, P. Danforth, R. Hurd, S. Severson, and J. Lloyd, "Recent science and engineering results with the laser guidestar adaptive optics system at Lick Observatory," in *Adaptive Optical System Technologies II*, P. L. Wizinowich and D. Bonaccini, eds., Proc. SPIE **4839,** 354–359 (2003).
10. D. L. Fried, "Optical resolution through a randomly inhomogeneous medium for very long and very short exposures," J. Opt. Soc. Am. **56,** 1372–1379 (1966).
11. M. Schoeck, D. Le Mignant, G. Chanan, P. L. Wizinowich, and M. A. van Dam, "Atmospheric characterization with the Keck adaptive optics system. I. Open-loop data," Appl. Opt. **42,** 3705–3720 (2003).
12. C. Neyman, W. M. Keck Observatory, 65-1120 Mamalahoa Highway, Kamuela, Hawaii (personal communiation, 2003).
13. R. H. Hudgin, "Wave-front reconstruction for compensated imaging," J. Opt. Soc. Am. **67,** 375–378 (1977).
14. B. L. Ellerbroek, A.U.R.A., 950 North Cherry Avenue, Tucson, Ariz., 85719 (personal communication, 2002).
15. B. R. Oppenheimer, D. Palmer, R. G. Dekany, A. Sivaramakrishnan, M. A. Ealey, and T. R. Price, "Investigating a Xinetics Inc. deformable mirror," in *Adaptive Optics and Applications*, R. K. Tyson and R. Q. Fugate, eds., Proc. SPIE **3126,** 569–580 (1997).
16. S. E. Winters, "Modeling and control of a deformable mirror," J. Dynamic Syst. Meas. Control **124,** 297–302 (2002).
17. D. S. Acton, P. L. Wizinowich, P. J. Stomski, J. C. Shelton, O. Lai, and J. M. Brase, "Laboratory calibration of the W. M. Keck Observatory adaptive optics facility," in *Adaptive Optical System Technologies*, D. Bonaccini and R. K. Tyson, eds., Proc. SPIE **3353,** 125–131 (1998).
18. M. D. Oliker, "Alignment techniques for DM, lenslet, and WFS camera at the SOR," in *Adaptive Optics and Applications*, R. K. Tyson and R. Q. Fugate, eds., Proc. SPIE **3126,** 595–604 (1997).
19. M. G. Loefdahl and G. B. Scharmer, "Wavefront sensing and image restoration from focused and defocused solar images," Astron. Astrophys. Suppl. Ser. **107,** 243–264 (1994).
20. R. J. Noll, "Zernike polynomials and atmospheric turbulence," J. Opt. Soc. Am. **66,** 207–211 (1976).
21. J.-P. Véran and G. Herriot, "Centroid gain compensation in Shack–Hartmann adaptive optics systems with natural or laser guide star," J. Opt. Soc. Am. A **17,** 1430–1439 (2000).
22. P. J. Stomski, Jr. and J. C. Shelton, "Compensating for pupil rotation in the W. M. Keck Observatory adaptive optics system," in *Adaptive Optical Systems Technology*, P. L. Wizinowich, ed., Proc. SPIE **4007,** 608–619 (2000).
23. N. F. Law and R. G. Lane, "Wavefront estimation at low light levels," Opt. Commun. **126,** 19–24 (1996).
24. P.-Y. Madec, "Control techniques," in *Adaptive Optics in Astronomy*, F. Roddier, ed. (Cambridge U. Press, Cambridge, UK, 1999), pp. 131–154.
25. P. D. Stroud, "Diffraction and scintillation of laser beams by atmospheric turbulence," Los Alamos National Laboratory Note LAUR-93-1401 (Los Alamos National Laboratory, Los Alamos, N. Mex., 1993).
26. R. Gerchberg and W. Saxton, "A practical algorithm for the determination of phase from image and diffraction plane picture," Optik **35,** 237–246 (1972).
27. R. G. Lane, W. R. Fright, and R. H. T. Bates, "Direct phase retrieval," IEEE Trans. Acoust. Speech Signal Process. **ASSP-35,** 520–526 (1987).
28. G. Chanan, C. Ohara, and M. Troy, "Phasing the mirror segments of the Keck telescopes. II. The narrowband phasing algorithm," Appl. Opt. **39,** 4706–4714 (2000).
29. E. M. Johansson, D. S. Acton, J. R. An, K. Avicola, B. V. Beeman, J. M. Brase, C. J. Carrano, J. Gathright, D. T. Gavel, R. L. Hurd, O. Lai, W. Lupton, B. A. Macintosh, C. E. Max, S. S. Olivier, J. C. Shelton, P. J. Stomski, K. Tsubota, K. E. Waltjen, J. A. Watson, and P. L. Wizinowich, "Initial performance of the Keck AO wavefront controller system," in *Adaptive Optical Systems Technology*, P. L. Wizinowich, ed., Proc. SPIE **4007,** 600–607 (2000). 30
30. F. J. Rigaut, J.-P. Véran, and O. Lai, "Analytical model for Shack–Hartmann-based adaptive optics systems," in *Adaptive Optical System Technologies*, D. Bonaccini and R. K. Tyson, eds., Proc. SPIE **3353,** 1038–1048 (1998).
31. F. Roddier, "The effect of atmospheric turbulence in optical astronomy," in *Progress in Optics*, E. Wolf, ed. (North-Holland, Amsterdam, 1981), Vol. 19, pp. 283–376.